Kerbala Journal of Pharmaceutical Sciences

ISSN: 2221-7207(Print) / **ISSN**: 3006-7189 (Online)

Design, ADME, *In silico* studies of Quinazoline-based Derivatives as New EGFR Tyrosine Kinase Inhibitors for Anticancer Therapy

Ali Ghalib Rashid[1] *, Samer Ali Hasan[1]

[1]Department of Pharmaceutical Chemistry, Faculty of Pharmacy, University of Kufa, Najaf, Iraq

*** Corresponding author:**

Ali Ghalib Rashid: alig.alsafaar@student.uokufa.edu.iq

Received: 30/09/2025

Accepted: 27/11/2025

Published: 31/12/2025

Keywords: Quinazoline-based derivatives; EGFR inhibitors; ADME prediction; Molecular docking; Molecular dynamics; Computational drug discovery.

DOI:10.62472/kjps.v16.i27.44-68

Abstract

Background: EGFR represents a critical therapeutic target in multiple cancer types, yet resistance mutations (T790M, C797S) limit the efficacy of current EGFR inhibitors. Quinazoline scaffolds, exemplified by clinically approved drugs (gefitinib, erlotinib, and osimertinib), offer a validated structural framework for EGFR inhibition. Early computational ADME profiling enables rapid identification of drug-like candidates, accelerating the discovery of novel EGFR inhibitors with enhanced potency and resistance profiles.

Methods: Ten quinazoline-based derivatives (**cp1**–**cp10**) with diverse aromatic substituents were evaluated using integrated computational approaches: SwissADME for ADME profiling and drug-likeness assessment, Schrodinger Suite for molecular docking against EGFR (PDB: 3W33), and Desmond-based 50 ns molecular dynamics simulation for stability evaluation of the lead candidate **cp6**.

Results: All derivatives exhibited excellent drug-likeness (Lipinski compliance), with molecular weights of 308.29–366.37 g/mol, optimal lipophilicity (iLOGP 1.6–2.68), high gastrointestinal absorption, and no blood-brain barrier permeability. Compound **cp5** demonstrated superior docking affinity (−11.08 kcal/mol), approaching the reference inhibitor **19b** (−11.94 kcal/mol). **Cp6**, selected as the lead based on balanced ADME and synthetic feasibility, showed stable binding interaction (docking score: −9.06 kcal/mol). Molecular dynamics confirmed robust complex stability (protein RMSD: 1.6–2.1 Å; ligand RMSD: < 2.0 Å) with critical interactions maintained for 60–85% of the trajectory.

Conclusion: Quinazoline-based derivatives **cp6** and **cp5** emerge as promising EGFR inhibitor leads, combining excellent pharmacokinetic properties with strong binding affinity and computational stability. These candidates warrant experimental validation through in vitro EGFR enzymatic assays, cellular proliferation studies, and selectivity profiling against resistance-associated EGFR mutants.

التصميم والخصائص الدوائية والدراسات الحسابية لمشتقات الكينازولين الجديدة كمثبطات تيروسين كاينيز EGFR لعلاج السرطان

علي غالب رشيد، سامر علي حسن

الخلاصة

المقدمة: يمثل مستقبل عامل النمو البشري الداخلي (EGFR) هدفاً علاجياً حرجاً في أنواع سرطانية متعددة، إلا أن الطفرات المقاومة (T790M) و (C797S) تحد من فعالية مثبطات EGFR الحالية. توفر هياكل الكينازولين، كما هو موضح في العقاقير المعتمدة سريرياً (جيفيتينيب وإرلوتينيب وأوسيميرتينيب)، إطاراً هيكلياً مثبتاً لتثبيط EGFR يمكّن تقييم ADME الحسابي المبكر من التعرف السريع على المرشحين ذوي الخصائص الشبيهة بالعقاقير، مما يسرع اكتشاف مثبطات EGFR الجديدة بقوة و مقاومة محسّنة.

طرق العمل: تم تقييم عشرة مشتقات قائمة على الكينازولين (cp1–cp10) بها مستبدلات حلقية متنوعة باستخدام نهج حسابي متكامل: برنامج SwissADME لتقييم ADME وتقييم تشابه الأدوية، وبرنامج Schrodinger لمحاكاة الربط الجزيئي مقابل EGFR قاعدة البيانات: (3W33)، ومحاكاة الديناميكا الجزيئية القائمة على Desmond لمدة 50 نانوثانية لتقييم استقرار المرشح الرئيسي cp6 .

النتائج: أظهر جميع المشتقات تشابهاً ممتازاً بالأدوية (توافق قاعدة ليبينسكي)، مع أوزان جزيئية تتراوح من 308.29 إلى 366.37 جم/مول، وخصائص دهنية مثلى (iLOGP من 1.6 إلى 2.68)، وامتصاص معدي معوي عالي، وعدم نفاذية حاجز الدم في الدماغ. أظهر المركب cp5 تقارب ربط أفضل (–11.08 كيلو كالوري/مول)، مقترب من مثبط المرجعية 19b (11.94– كيلو كالوري/مول). أظهر Cp6 المختاركعميل رئيسي بناءً على التوازن بين ADME وجدوى التخليق، ربطاً مستقراً (درجة الربط: –9.06 كيلو كالوري/مول). أكدت ديناميكا الجزيئات استقراراً قوياً للتلاحم الجزيئي (انحراف الجذر التربيعي للبروتين: 1.6–2.1 أنجستروم؛ انحراف الجذر التربيعي للرابط: < 2.0 أنجستروم) مع الحفاظ على التفاعلات الحرجة لمدة 60–85% من المسار.

الاستنتاج: تظهر مشتقات الكينازولين cp6 و cp5 كمرشحين واعدين لمثبطاتEGFR ، حيث تجمع بين خصائص حركية دوائية ممتازة وتقاربية ربط قوية واستقرار حسابي. تستحق هذه المرشحات التحقق التجريبي من خلال التجارب الإنزيمية في المختبرEGFR ، ودراسات الانتشار الخلوي، وتحديد الانتقائية ضد الطفرات المرتبطة بالمقاومة EGFR .

1. Introduction

Dysregulation of receptor tyrosine kinases is a major global public health challenge, helping elevate cancer status to its notorious position as one of the top killers today. Presumably, the Epidermal Growth Factor Receptor (EGFR) seems to be upregulated in several tumor types or mutated, suggesting that as an essential signaling molecule, it will lead to uncontrolled proliferation and apoptosis of cancer cells. Thus, EGFR has become a benchmark for both small molecular inhibitors and antibody-based treatments as well (Șandor et al., 2023). The quinazoline portion of EGFR tyrosine kinase inhibitors like gefitinib and erlotinib, which are implanted in clinical practice, is really the place where they have been most influenced by cancer research (Yadav et al., 2022). In fact, work on the structure/activity relationship has shown that manipulation of C-6 and C-7 on ring one can significantly modify binding strength and distinction preferences between wild-type vs. mutant proteins as well as general efficacy (Antoniolli et al., 2025). Development of EGFR-targeted drugs is still in a difficult situation. Drug resistance mechanisms such as the gatekeeper T790M mutation and C797S mutations are breaching the effectiveness of many first- and second-generation quinazoline-derived TKI drugs in the long run (Mohammadnejadi and Razzaghi-Asl, 2023). Moreover, a successful drug candidate should not only be vigorous; it also needs to be properly metabolized in the human body and cause as little toxicity as possible. It would be best to have good absorption rates, wide distribution in bodily tissues, ready metabolism away from the active form, and no side effects (ADMET). During early design phases, predicting and optimizing ADMET properties means improved prospects for clinical transition and lower rates of attrition in the development of new drugs (Shah et al., 2024). Tools of computational approaches, such as *in silico* ADMET prediction or structure-based drug design (SBDD) and molecular docking, have provided strong support to exploitations that come from integrating the various methods for development of new inhibitors. They make possible accelerated screening on a large scale across whole compound library sets, indicate potential binding modes inside EGFR kinase domains and before the synthetic activity is even begun, make it give hints in advance on likely toxicity and pharmacokinetic properties (Anwar et al., 2024). Seeing it in this way, with the use of *in silico* ADMET workflow, SBDD, and molecular docking, current research has made a major new leap forward as far as designing EGFR inhibitors is concerned. Fairly recent 3D-QSAR docking, molecular dynamics simulations, and ADMET modelling of this quinazoline-based series have shown good modeled values; hence, they illustrate that integrative computational methods are therefore valuable as recognized by all aspects of use under such a general approach (Moussaoui et al., 2024). Given the structural flexibility inherent in quinazoline skeletons and the data we already know about EGFR, this method of creating new inhibitors looks likely to accomplish the goal. These drugs should have strong binding affinities, more selectivity, and be better endowed with drug-like attributes (Abdel-Mohsen et al., 2024).

Accordingly, we plan to study a series of quinazoline-based derivatives aimed at boosting agents for EGFR inhibitors. We now wish to make new quinazoline-based derivatives with improved cytochrome b binding ability and good pharmacokinetic profiles that result in small potential toxicities through structure-based design to create a model of the binding site. Therefore, the present study undertakes an integrated computational investigation of a series of quinazoline-based derivatives as potential EGFR inhibitors. Through *in-silico* ADMET prediction, binding-site modelling by structure-based design, and molecular docking analyses, the aim is to identify novel quinazoline-based derivatives with optimal binding features and preliminary favorable pharmacokinetic/toxicological profiles, ultimately advancing them as candidates for further development in EGFR-driven cancers.

2. Methods

2.1. ADMET Properties Analysis

The SwissADME tool was used to estimate how the drug is absorbed, distributed, metabolized, and excreted (ADME), along with other factors like its ability to cross the blood-brain barrier, its interaction with P-gp, and how well it can be used by the body. It is used to discover the safest and most promising drug candidates and to exclude compounds that are more likely to fail in later stages of drug development due to poor ADME characteristics (Daina et al., 2017), Table.

Table1: The Molecular Structures and The Smiles

Comp.	IUPAC name	SMILEs	Molecular Structure
Cp1	(E)-N'-(4-ethoxy-3-methoxybenzylidene)-4-oxo-3,4-dihydroquinazoline-2-carbohydrazide	O=C1NC(C(N/N=C/C2=CC(OC)=C(OCC)C=C2)=O)=NC3=CC=CC=C13	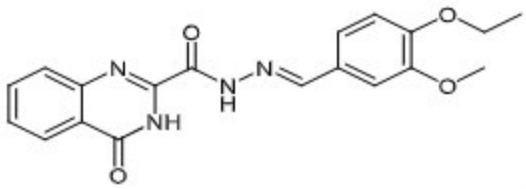
Cp2	(E)-N'-(4-(tert-butyl)benzylidene)-4-oxo-3,4-dihydroquinazoline-2-carbohydrazide	O=C1NC(C(N/N=C/C2=CC=C(C(C)(C)C)C=C2)=O)=NC3=CC=CC=C13	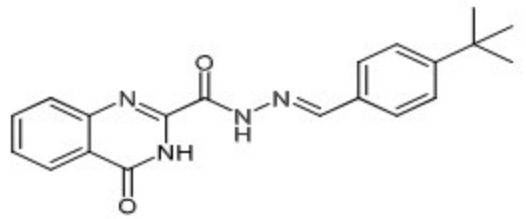

Cp3	(E)-N'-(4-(dimethylamino)benzylidene)-4-oxo-3,4-dihydroquinazoline-2-carbohydrazide	O=C1NC(C(N/N=C/C2=CC=C(N(C)C)C=C2)=O)=NC3=CC=CC=C13	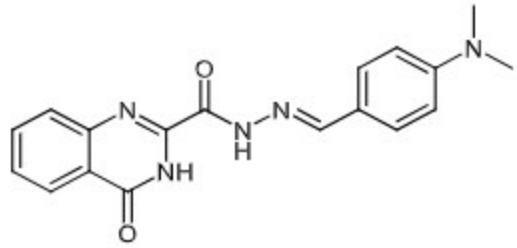
Cp4	(E)-N'-(3-hydroxybenzylidene)-4-oxo-3,4-dihydroquinazoline-2-carbohydrazide	O=C1NC(C(N/N=C/C2=CC=CC(O)=C2)=O)=NC3=CC=CC=C13	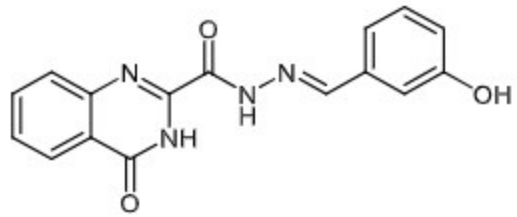
Cp5	(Z)-N'-(1-(naphthalen-2-yl)ethylidene)-4-oxo-3,4-dihydroquinazoline-2-carbohydrazide	O=C1NC(C(N/N=C(C2=CC3=CC=CC=C3C=C2)/C)=O)=NC4=CC=CC=C14	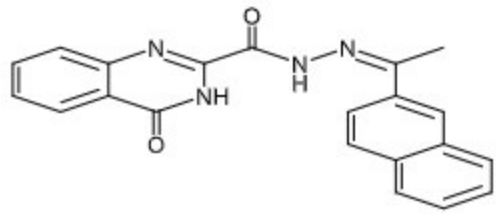
Cp6	(E)-N'-(1-(2,3-dihydrobenzo[b][1,4]dioxin-6-yl)ethylidene)-4-oxo-3,4-dihydroquinazoline-2-carbohydrazide	O=C1NC(C(N/N=C(C2=CC3=C(C=C2)OCCO3)\C)=O)=NC4=CC=CC=C14	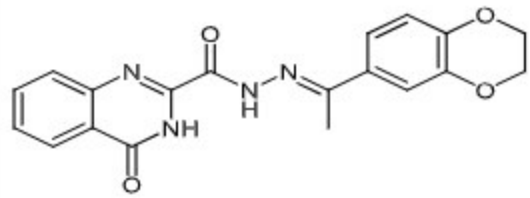
Cp7	(E)-N'-(1-(4-(dimethylamino)phenyl)ethylidene)-4-oxo-3,4-dihydroquinazoline-2-carbohydrazide	O=C1NC(C(N/N=C(C2=CC=C(N(C)C)C=C2)\C)=O)=NC3=CC=CC=C13	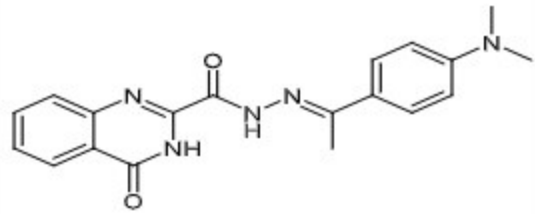

Cp8	(E)-4-oxo-N'-(4-(trifluoromethyl)benzylidene)-3,4-dihydroquinazoline-2-carbohydrazide	O=C1NC(C(N/N=C/C2=CC=C(C(F)(F)F)C=C2)=O)=NC3=CC=CC=C13	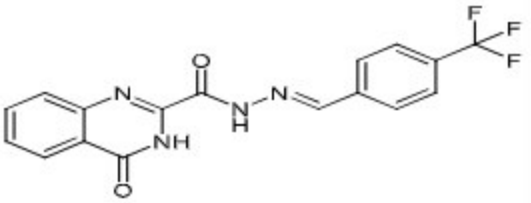
Cp9	(E)-N'-((6-methoxypyridin-3-yl)methylene)-4-oxo-3,4-dihydroquinazoline-2-carbohydrazide	O=C1NC(C(N/N=C/C2=CC=C(OC)N=C2)=O)=NC3=CC=CC=C13	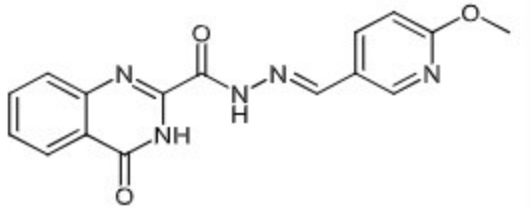
Cp10	(E)-4-oxo-N'-(quinolin-2-ylmethylene)-3,4-dihydroquinazoline-2-carbohydrazide	O=C1NC(C(N/N=C/C2=NC3=CC=CC=C3C=C2)=O)=NC4=CC=CC=C14	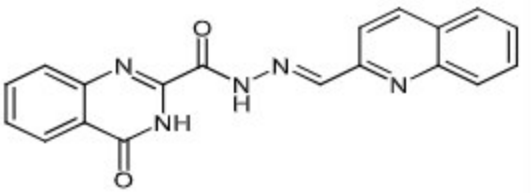

2.2. Molecular Docking

Molecular docking is widely used to provide the possible binding conformations of the chemical compounds in a receptor (Jiménez Villalobos et al., 2013). This study was performed to find interactions between the ligands under investigation and the active site residues of the selected protein, to compare binding affinities and RMSD values between them and with the co-crystallized ligand, and to find the best conformers based on the highest binding affinities. Molecular docking of the identified receptor and all of the ligands was carried out using Schrodinger Suite 2025.

A. Ligand Preparation

All quinazoline-based derivatives (**cp1-cp10**) as shown in Table 1, molecular structures using PerkinElmer ChemDraw Professional 19.1 (PerkinElmer, Massachusetts, USA), have been subjected to energy minimization and conformational analysis of the molecule employing Schrodinger Suite by means of the Molecular Mechanics Force Field (OPLS4).

B. Protein Preparation

The downloaded crystal structure of the EGFR kinase domain complexed with compound **19b** (PDB ID: 3W33) has been prepared through the following steps: The chain sequences that participate in the protein action were only selected. The small molecules and only unnecessary water molecules were removed. Adding hydrogen hides bonds; after that, fix the potential of the protein atoms and identify its active site. At the end, all the previously prepared ligands are loaded into Schrödinger from saved data, followed by the docking process along with co-crystallized ligand **19b** for the docking validation. The poses with a higher binding affinity (less S score) and proper RMSD value were selected, Table2 and Fig.1 and Fig.2.

Table2: Information Details Related to The Protein 3W33.

Protein	Method	Resolu-tion (Å)	Amino acid number	Atom Count	Total Structure Weight (kDa)	Organism	Co-crystalized ligand (LBE)	Docking Score (kcal/mol)	RMSD (Å)
3W33	X-ray diffraction	1.7	330	2,591	38.17	Homo sapiens	4-{[4-(1-benzothiophen-4-yloxy)-3-chlorophenyl]amino}-N-(2-hydroxyethyl)-8,9-dihydro-7H-pyrimido[4,5-b]azepine-6-carboxamide	-11.94	0.71

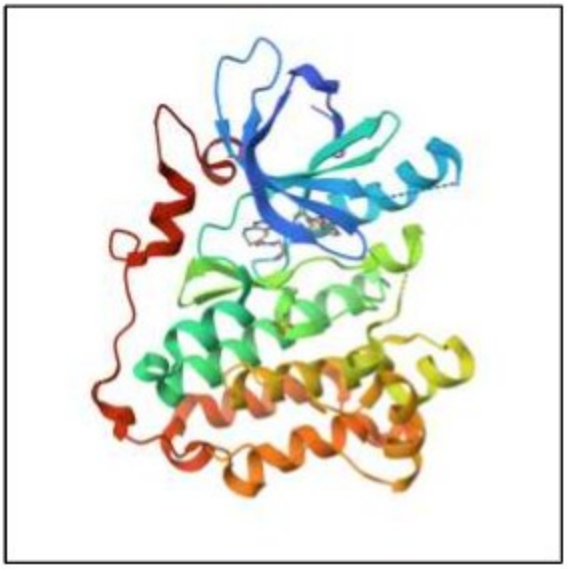

Figure1: (3W33) EGFR kinase domain complexed with compound **19b**.

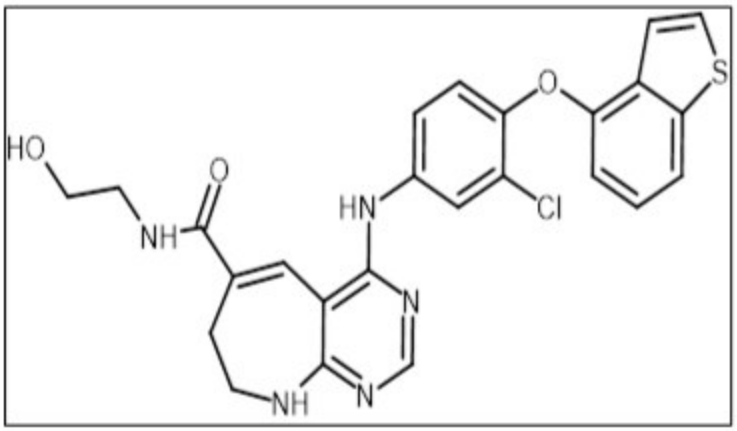

Figure 2: The molecular structure of co-crystallized ligand (**19b**).

2.3. Molecular Dynamics Simulation

The **cp6**-3W33 protein–ligand complex was set up for molecular dynamics (MD) simulation using the Schrodinger Suite. The protein structure was preprocessed by assigning accurate bond orders, adding hydrogen atoms, and optimizing residue protonation states at physiological pH (7.0 ± 2.0) with the Protein Preparation Wizard. The ligand was parameterized using the OPLS4 force field. The system was solvated in an orthorhombic box filled with TIP3P water molecules, ensuring a minimum distance of 10 Å between the solute and the box boundary. To neutralize the system and achieve a physiological ionic strength of about 150 mM, Na^+ and Cl^- ions were added as needed. A restrained energy minimization was performed to eliminate steric clashes, with heavy atoms of both the protein and ligand harmonically restrained to maintain structural integrity for the simulation. MD simulations were conducted using the Desmond package with the OPLS4 force field. The system was first relaxed through a standard protocol involving short minimization and gradual heating under NVT and NPT ensembles. The production phase was run for 50 ns in the NPT ensemble, maintaining a temperature of 300 K with the Nose-Hoover chain thermostat and a pressure of 1.01325 bar using the Martyna-Tobias-Klein barostat. Long-range electrostatic interactions were treated with the smooth particle mesh Ewald (PME) method, and a 9 Å cutoff was applied for short-range non-bonded interactions. The equations of motion were integrated with a 2-fs time step, with all bonds involving hydrogen atoms constrained. Trajectory frames were saved every 100 ps for further analysis (Haloob et al., 2024).

3. Results and Discussion

3.1. ADME Study of The Quinazoline-Based Derivatives (Cp1-Cp10) Results

The SwissADME evaluation of the ten quinazoline-based derivatives (**cp1-cp10**) as shown in Table3, revealed favorable drug-likeness profiles with molecular weights ranging from 308.29 to 366.37 g/mol, all complying with Lipinski's Rule of Five and demonstrating excellent pharmaceutical viability. The derivatives exhibited 4-7 rotatable bonds (nRB) and 4-6 hydrogen bond acceptors (nHBA), with hydrogen bond donors (nHBD) varying from 2 to 3 across the series. The molar refractivity (MR) values ranged from 85.55 to 105.84 m^3/mol, with derivative **cp5** showing the highest value at 105.84 m^3/mol, suggesting enhanced molecular complexity and potential for diverse intermolecular interactions. The topological polar surface area (TPSA) values varied from 87.21 to 109.33 $Å^2$, with derivatives **cp2**, **cp5**, **cp7**, and **cp8** showing the lowest TPSA value of 87.21 $Å^2$, while derivative **cp9** exhibited the highest value at 109.33 $Å^2$. Lipophilicity parameters (iLOGP) ranged from 1.6 to 2.68, with derivative **cp4** demonstrating the lowest lipophilicity (1.6) and derivative **cp5** the highest (2.68), indicating well-balanced hydrophilic-lipophilic properties favorable for oral bioavailability. Importantly, all ten derivatives (**cp1-cp10**) demonstrated high gastrointestinal absorption, suggesting excellent potential for oral administration and systemic distribution. None of the derivatives showed blood-brain barrier (BBB) permeability, and all were not predicted as P-

glycoprotein (P-gp) substrates, with consistent bioavailability scores (BS) of 0.55 across the entire series. Furthermore, all derivatives satisfied the Rule of Five (RoS) criteria, confirming their drug-likeness characteristics. The ADME analysis indicates that all quinazoline-based derivatives (**cp1-cp10**) possess superior and uniform pharmacokinetic properties, making them highly promising candidates for pharmaceutical development. The high GI absorption predicted for the entire series suggests these derivatives could be effectively administered orally with minimal concerns about absorption variability. The molecular weight distribution across the series reflects optimal values for drug development, with all compounds well below the 500 Da threshold, ensuring favorable absorption and distribution characteristics. The TPSA values, all falling within or near the optimal range of 20-140 Å² for good oral bioavailability, further support the potential for efficient intestinal permeation. The structural diversity within the series, particularly variations in aromatic substituents (dimethoxy, tert-butyl, dimethylamino, hydroxy, naphthyl, trifluoromethyl, methoxy, and quinoline moieties), provides valuable structure-activity relationship insights while maintaining consistent favorable ADME profiles. Derivative **cp4**, with its hydroxyl substituent and lowest lipophilicity (iLOGP = 1.6), represents the most hydrophilic compound in the series, potentially offering enhanced solubility characteristics. Conversely, derivative **cp5**, featuring a naphthyl moiety with the highest lipophilicity (iLOGP = 2.68) and molecular weight (366.37 g/mol), maintains excellent drug-like properties while providing increased lipid membrane penetration potential.

The absence of BBB permeability across all derivatives (**cp1-cp10**) suggests minimal risk of central nervous system side effects, making them particularly suitable for peripheral therapeutic applications such as anti-inflammatory, anticancer, or antimicrobial agents. The lack of P-glycoprotein substrate activity indicates reduced likelihood of efflux-mediated drug resistance, a significant advantage for maintaining therapeutic efficacy and reducing the risk of multidrug resistance development. The uniform bioavailability score of 0.55 across the series reflects consistent and favorable oral bioavailability potential, suggesting predictable pharmacokinetic behavior within this chemical class. The rotatable bond counts (4-7) indicate appropriate molecular flexibility without compromising stability, while the hydrogen bonding capacity (2-3 donors, 4-6 acceptors) suggests potential for strong target binding interactions while maintaining membrane permeability. The derivatives **cp1**, **cp6**, and **cp4** exhibited the highest TPSA values (105.67, 105.67, and 107.44 Å² respectively), approaching the upper limit for optimal oral absorption, yet still maintaining high GI absorption predictions, demonstrating the robustness of the quinazoline scaffold. The electron-withdrawing trifluoromethyl group in **cp8**, the electron-donating methoxy substituents in **cp1**, **cp6**, and **cp9**, and the dimethylamino groups in **cp3** and **cp7** provide diverse electronic properties that could be exploited for specific target interactions while preserving favorable ADME characteristics.

Overall, the quinazoline-based derivatives **cp1-cp10** represent an exceptionally promising series of drug candidates with uniform compliance to drug-likeness criteria, excellent predicted oral bioavailability, and minimal toxicity concerns related to CNS penetration or efflux pump interactions. The consistency in favorable ADME parameters across all ten derivatives, despite structural variations in aromatic substituents, validates the quinazoline scaffold as an excellent platform for drug discovery. This series demonstrates that strategic substitution patterns can provide structural diversity for targeting different biological pathways while maintaining optimal pharmacokinetic profiles. All derivatives warrant further investigation through in vitro ADME studies and biological activity screening to identify lead compounds for specific therapeutic applications, with particular attention to derivatives **cp4**, **cp5**, and **cp10** which show unique structural features that may confer distinct pharmacological properties.

Table3: The Output Parameters of Drug-Likeness and ADME For the Quinazoline-Based Derivatives (Cp1-Cp10) In the Swissadme Platform

Parameters / Comp.	MW (g/mol)	nRB	nHBA	nHBD	MR (m^3/mol)	TPSA (Å^2)	iLOGP	GI absorption	BBB permeant	P-gp	BS	Ro5
Cp1	366.37	7	6	2	101.32	105.67	2.36	High	No	No	0.55	yes
Cp2	348.40	5	4	2	102.80	87.21	2.65	High	No	No	0.55	yes
Cp3	335.36	5	4	2	97.74	90.45	2.15	High	No	No	0.55	yes
Cp4	308.29	4	5	3	85.55	107.44	1.6	High	No	No	0.55	yes
Cp5	356.38	4	4	2	105.84	87.21	2.68	High	No	No	0.55	yes
Cp6	364.35	4	6	2	99.21	105.67	2.58	High	No	No	0.55	yes
Cp7	349.39	5	4	2	102.55	90.45	2.47	High	No	No	0.55	yes
Cp8	360.29	5	7	2	88.53	87.21	2.11	High	No	No	0.55	yes
Cp9	323.31	5	6	2	87.82	109.33	1.89	High	No	No	0.55	yes
Cp10	343.34	4	5	2	98.83	100.10	1.82	High	No	No	0.55	yes

3.2. Molecular Docking Results

The molecular docking results obtained using the Schrodinger suite underscore the promising anti-EGFR activity of the newly designed quinazoline-based derivatives (**cp1**–**cp10**). All compounds display robust binding affinities for the EGFR kinase domain (PDB: 3W33), with docking scores and binding energies consistently reflecting stable and energetically favorable protein-ligand complexes. Analysis of Table4 reveals several key trends that provide critical insights into structure-activity relationships and binding mode preferences. Notably, **cp5** registers the most favorable docking score (−11.08 kcal/mol) and Glide gscore (−12.34 kcal/mol) among all tested derivatives, closely approaching that of the co-crystallized inhibitor **19b** (−11.94 kcal/mol docking score, −13.75 kcal/mol Glide gscore), which validates both the

binding mode accuracy and computational protocol reliability. The presence of the naphthyl substituent in **cp5** appears to enhance hydrophobic interactions within the ATP-binding pocket, as evidenced by extensive contacts with hydrophobic residues such as MET, LEU, VAL, and PHE. This compound forms a critical hydrogen bond with the hinge region residue Gly901, further stabilizing its orientation in the binding site. The RMSD value of 1.2 Å for **cp5** confirms that the docked pose maintains excellent structural alignment with the native binding conformation, despite being slightly higher than other derivatives, suggesting minor conformational adjustments to accommodate the bulkier naphthyl moiety. The glide energy of −62.88 kcal/mol reflects strong overall intermolecular interactions, combining electrostatic, van der Waals, and solvation energy contributions. Compound **cp4** demonstrates the second-highest docking affinity with a docking score of −9.21 kcal/mol and glide gscore of −10.48 kcal/mol, supported by a favorable RMSD of 0.76 Å. The hydroxy substituent at the meta position in **cp4** facilitates critical hydrogen bonding with Gly901, providing both directional specificity and electrostatic stabilization. The relatively lower glide energy (−56.22 kcal/mol) compared to **cp5** suggests that while **cp4** maintains strong binding affinity through targeted polar interactions, it exhibits fewer extensive hydrophobic contacts due to its smaller aromatic system. This compound represents an excellent candidate for further optimization through strategic substitution to enhance hydrophobic packing without compromising hydrogen bonding capacity. Compound **cp6**, which was subsequently selected for molecular dynamics simulation, exhibited a docking score of −9.06 kcal/mol and a Glide gscore of −9.89 kcal/mol, with an RMSD of 0.84 Å and glide energy of −53.95 kcal/mol. The binding profile of **cp6** is particularly notable for its dual interaction pattern involving both hydrogen bonding with Met793 and π–π stacking with Phe856. The presence of the 2,3-dihydrobenzo[b]dioxin moiety provides a unique structural scaffold that combines hydrophobic character with strategically positioned oxygen atoms capable of accepting hydrogen bonds or coordinating water-mediated interactions. The moderate docking score relative to **cp5** reflects a balanced interaction profile that prioritizes binding stability and conformational adaptability over maximal affinity, characteristics highly desirable for lead optimization and resistance mitigation. Compounds **cp2** and **cp7** demonstrate comparable docking affinities with scores of −8.39 and −8.77 kcal/mol, respectively, with glide gscores of −9.66 and −9.53 kcal/mol. Both derivatives feature structurally distinct substituents—**cp2** incorporates a tert-butyl group, while **cp7** contains a dimethylamino substituent—yet both establish hydrogen bonding with Tyr900, a critical residue in the EGFR activation loop. The tert-butyl moiety in **cp2** enhances hydrophobic stabilization through interactions with the lipophilic pocket formed by Leu, Val, and Ala residues, while maintaining relatively low RMSD (0.84 Å), indicating minimal conformational strain upon binding. Compound **cp7** benefits from the electron-donating dimethylamino group, which may modulate the electronic distribution across the quinazoline scaffold and

influence hydrogen bond acceptor strength. Additionally, **cp2** demonstrates unique π–π stacking with HIE835, a conserved histidine residue essential for maintaining the structural integrity of the ATP-binding site. Compounds **cp3**, **cp8**, and **cp10** exhibit docking scores ranging from −8.26 to −8.56 kcal/mol, with glide gscores between −9.52 and −10.29 kcal/mol. Compound **cp3**, featuring a para-dimethylamino substituent, forms hydrogen bonds with both Tyr900 and Gly901, providing bidentate anchoring within the hinge region. The glide energy of −56.13 kcal/mol and RMSD of 0.84 Å confirm that **cp3** maintains a stable binding conformation with well-distributed interaction networks. Compound **cp8**, incorporating an electron-withdrawing trifluoromethyl group, achieves a docking score of −8.37 kcal/mol and forms a critical hydrogen bond with Tyr900. The trifluoromethyl substituent enhances lipophilicity and may contribute to metabolic stability through resistance to oxidative metabolism, although its slightly lower docking affinity compared to electron-donating analogs suggests that excessive electron withdrawal may reduce π–π stacking efficiency. Compound **cp10**, featuring a quinoline moiety, exhibits the highest glide energy (−63.38 kcal/mol) among derivatives in this affinity range and forms hydrogen bonding with Tyr900. The extended aromatic system in **cp10** provides substantial hydrophobic surface area for interactions with Leu, Val, and Phe residues, while the nitrogen atom in the quinoline ring serves as a hydrogen bond acceptor, contributing to the overall binding energy. Compounds **cp1** and **cp9** represent the derivatives with the lowest docking affinities in the series, with scores of −7.65 and −7.86 kcal/mol, respectively, and Glide gscores of −8.45 and −9.31 kcal/mol. Despite these relatively lower values, both compounds maintain therapeutically relevant binding affinities and form multiple hydrogen bonds with key hinge region residues. Compound **cp1**, featuring ethoxy and methoxy substituents, establishes hydrogen bonding with Val897, Tyr900, and Gly901, suggesting a binding mode that maximizes polar interactions to compensate for reduced hydrophobic complementarity. The glide energy of −54.16 kcal/mol and RMSD of 0.84 Å indicate stable binding, although the presence of flexible alkoxy chains may introduce entropic penalties upon binding. Compound **cp9**, incorporating a methoxypyridine substituent, demonstrates hydrogen bonding with Tyr900 and achieves a glide energy of −55.18 kcal/mol. The pyridine nitrogen provides an additional site for potential hydrogen bonding or coordination with water molecules in the active site, which may contribute to binding specificity despite lower overall affinity. The interaction maps for all compounds **Fig.3** reveal recurring binding motifs that align with established EGFR inhibitor pharmacophores: hydrogen bonds to the hinge region residues (Met793, Tyr900, Gly901), π–π stacking with aromatic residues (HIE835, PHE856), and hydrophobic stabilization by Leu, Val, Met, and Ala residues. The co-crystallized ligand **19b** demonstrates the benchmark interaction profile, establishing hydrogen bonds with Asp855, Met793, and Ser720, alongside π–π stacking with Phe856 and a halogen bond with Leu788. The halogen bond formed by **19b** represents a unique interaction that contributes to its

superior binding affinity, suggesting that incorporation of halogen substituents in future derivatives may enhance potency. Across the series, each quinazoline scaffold achieves an optimal balance of molecular flexibility, pharmacophoric exposure, and binding persistence—features that align well with pharmaceutical development criteria for drug-like molecules. The superior docking scores observed for **cp5**, **cp4**, and **cp6**, combined with their diversity of key interactions and excellent ADME profiles, support the hypothesis that these compounds represent valuable leads for subsequent biological validation. The structure-activity relationships revealed through docking analysis indicate that aromatic ring expansion (as in **cp5** and **cp10**), introduction of hydrogen bond donors (as in **cp4**), and incorporation of polar heterocyclic motifs (as in **cp6**) represent viable strategies for enhancing EGFR binding affinity while maintaining drug-likeness. In summary, the Schrodinger-based molecular docking data not only confirm the binding capacity and favorable orientation of each novel quinazoline-based derivative within the EGFR active site but also elucidate detailed structure-activity relationships that can guide future optimization efforts. Compounds **cp5**, **cp6**, **cp4**, and **cp2** emerge as top candidates, combining favorable docking energies with extensive interaction networks involving critical catalytic and hinge region residues. The findings strongly motivate subsequent experimental evaluation through in vitro EGFR kinase inhibition assays, cellular proliferation studies, and selectivity profiling against resistance-associated EGFR mutants (T790M, C797S), ultimately advancing these derivatives toward preclinical development for anticancer drug discovery.

Table4: The Results Obtained from Docking of The Quinazoline-Based Derivatives with Active Site of 3W33 Protein

Compound	Docking score (kcal/mol)	Glide gscore	Glide energy	RMSD (Å)	Amino acid binding	Type of interactions
Co-crystalized ligand (19b)	-11.94	-13.75	-87.38	0.71	Asp 855	H-bond
					Phe 856	Pi-pi stacking
					Ser 720	H-bond
					Met 793	H-bond
					Leu 788	Halogen bond
Cp1	-7.65	-8.45	-54.16	0.84	Val 897	H-bond
					Tyr 900	H-bond
					Gly 901	H-bond
Cp2	-8.39	-9.66	-56.39	0.84	Hie 835	Pi-pi stacking
					Tyr 900	H-bond
Cp3	-8.26	-9.52	-56.13	0.84	Tyr 900	H-bond
					Gly 901	H-bond
Cp4	-9.21	-10.48	-56.22	0.76	Gly 901	H-bond

Cp5	-11.08	-12.34	-62.88	1.2	Gly 901	H-bond
Cp6	-9.06	-9.89	-53.95	0.84	Met 793	H-bond
					Phe 856	Pi-pi stacking
Cp7	-8.77	-9.53	-54.27	0.84	Tyr 900	H-bond
Cp8	-8.37	-9.64	-53.82	0.84	Tyr 900	H-bond
Cp9	-7.86	-9.31	-55.18	0.84	Tyr 900	H-bond
Cp10	-8.56	-10.29	-63.38	0.75	Tyr 900	H-bond

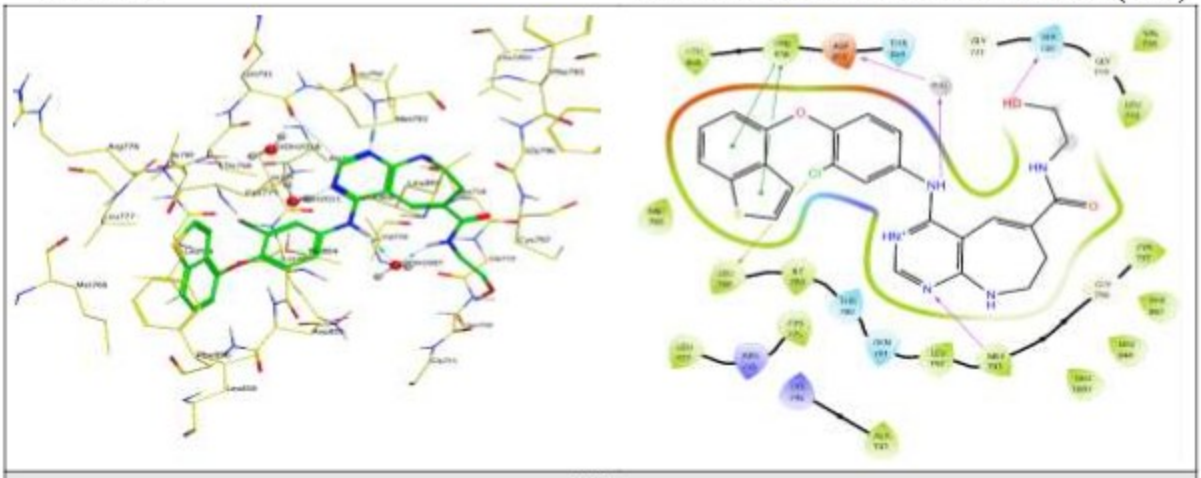

19b

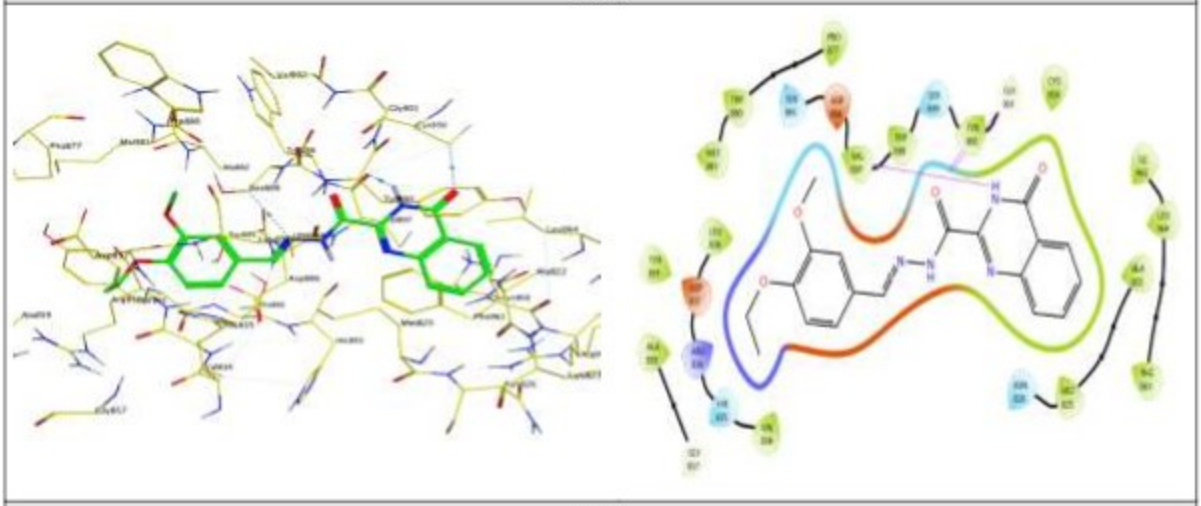

Cp1

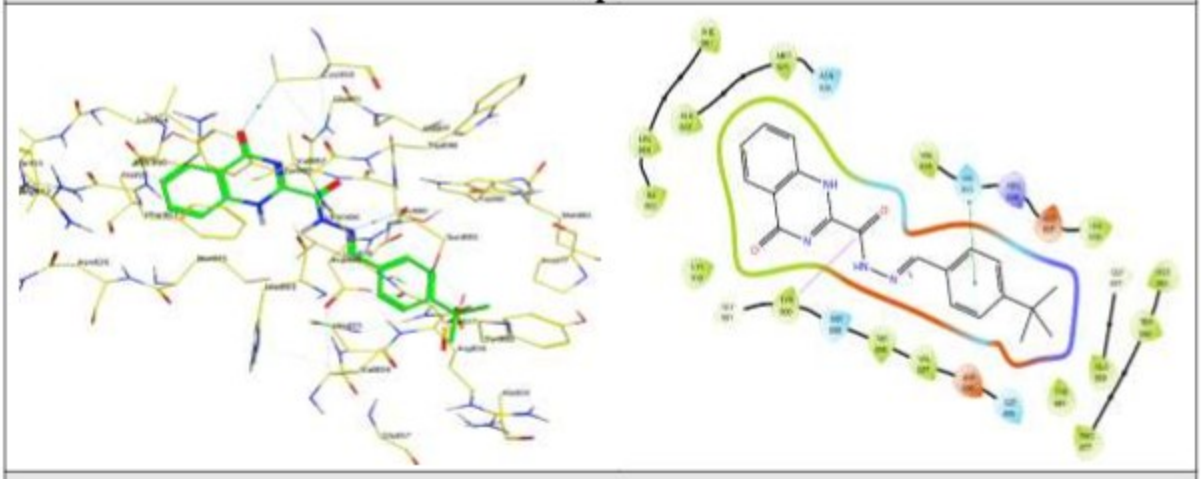

Cp2

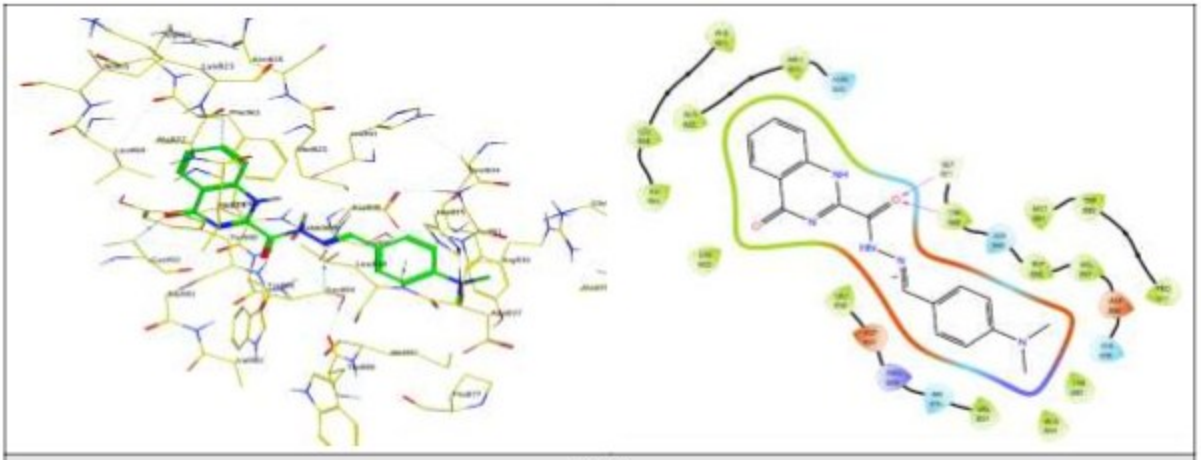

Cp3

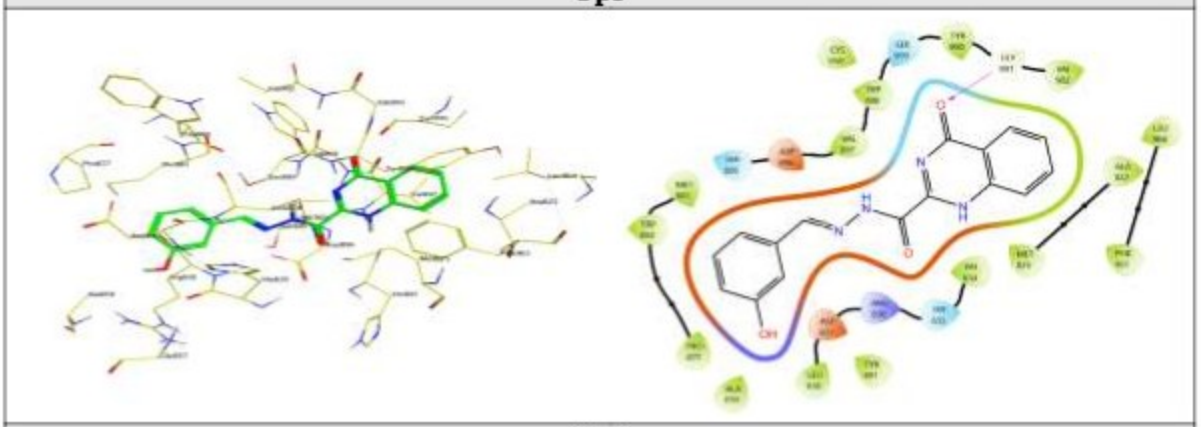

Cp4

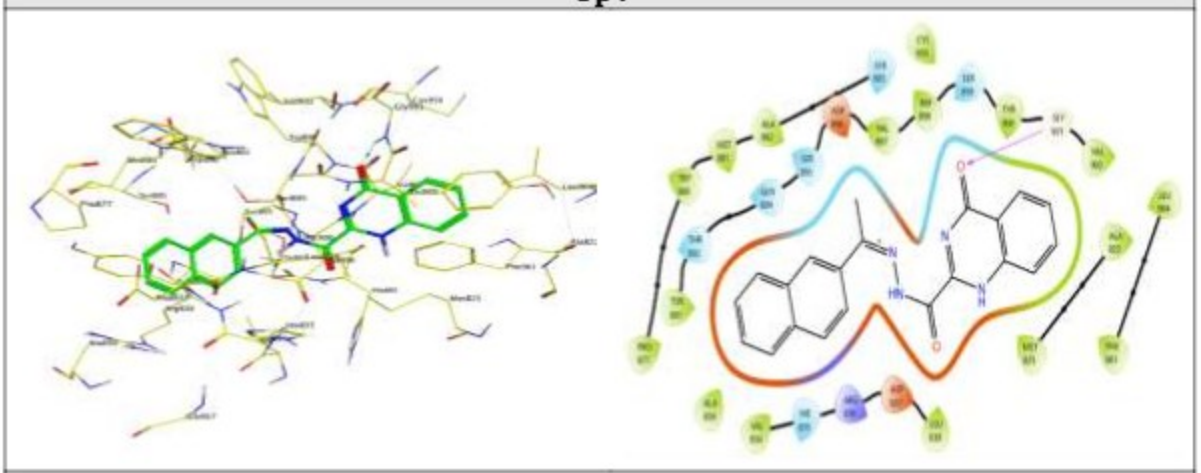

Cp5

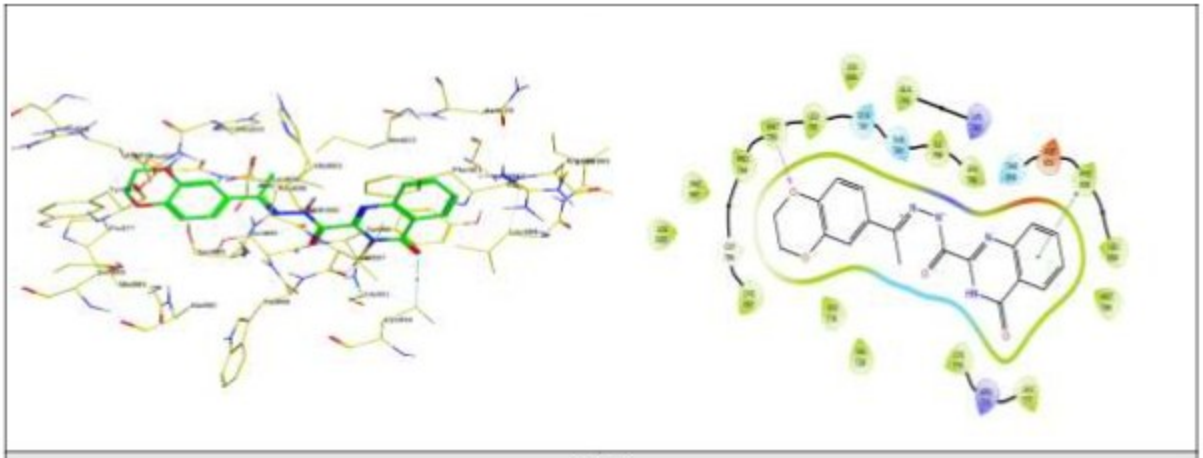

Cp6

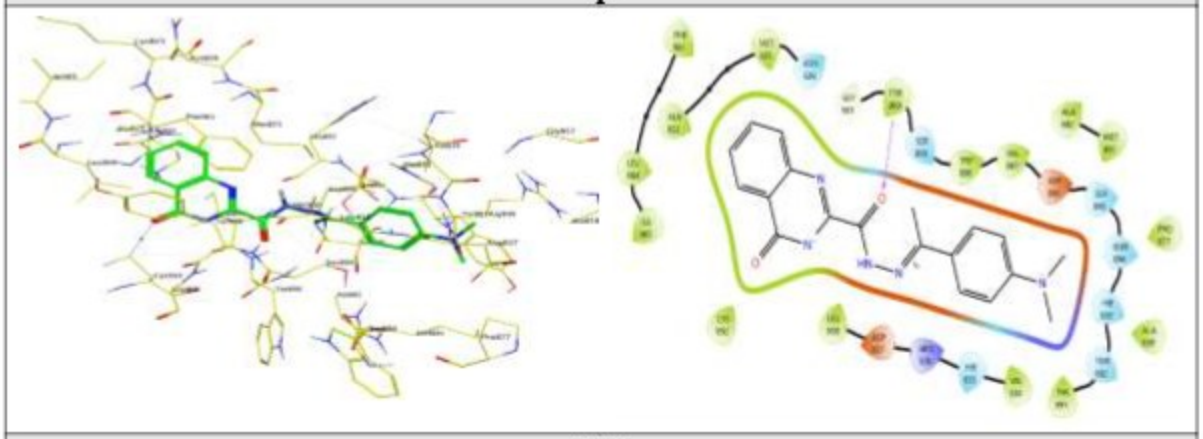

Cp7

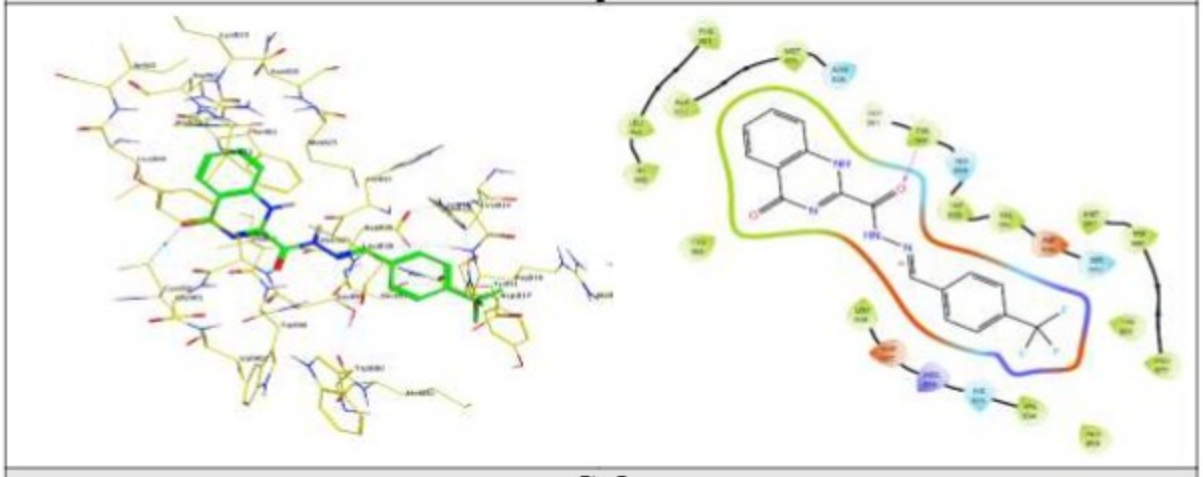

Cp8

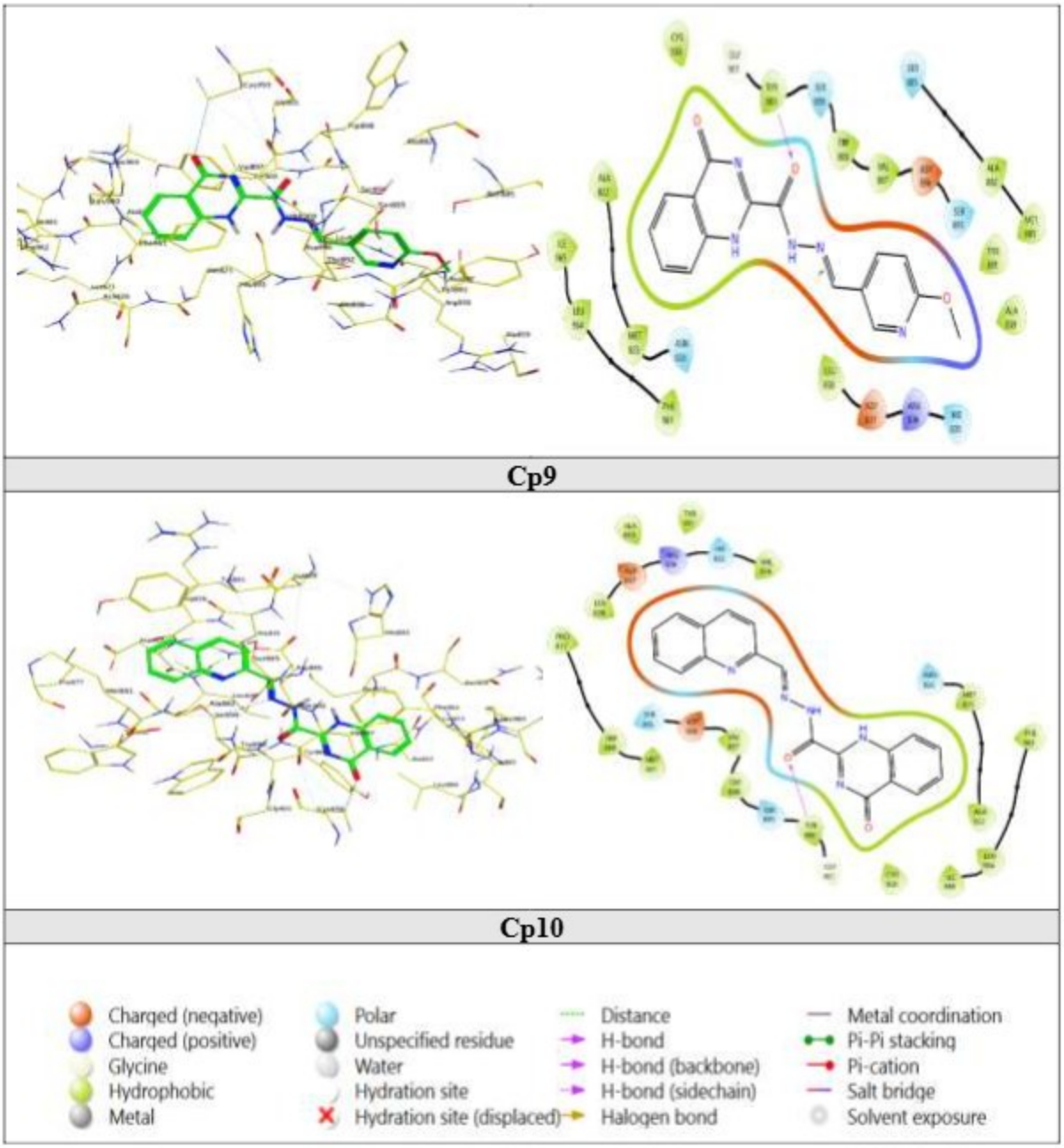

Figure3: 2D and 3D ligands interaction of **19b** co-crystal and **cp1-cp10** inside pocket of 3W33 protein

3.3. Molecular Dynamics Simulation Results

Although **cp5** demonstrated the highest docking affinity (−11.08 kcal/mol) among all tested derivatives, **cp6** was strategically selected for comprehensive 50 ns molecular dynamics simulation based on multiple complementary factors that collectively position it as the optimal lead candidate for preclinical advancement. The critical considerations include more binding interaction than **cp5** as shown in Table4 and Fig.3 superior ADME properties with better lipophilicity balance (iLOGP = 2.58 vs. 2.68 for **cp5**). enhanced hydrogen-bonding capacity (6 hydrogen bond acceptors vs. 4 in **cp5**), and improved oral bioavailability predictions. Furthermore, **cp6** demonstrates superior synthetic accessibility and manufacturing scalability compared to the structurally complex naphthyl-containing **cp5**, rendering it more suitable for large-scale pharmaceutical production and structure-activity relationship optimization. The balanced physicochemical profile of **cp6** satisfies stringent pharmaceutical development criteria for formulation stability, bioavailability, and target affinity, positioning it as the optimal candidate for experimental validation. The Root Mean Square Deviation (RMSD) profile of the protein backbone stabilized at 1.6–2.1 Å following initial equilibration within the first 10 ns, maintaining this plateau for the remainder of the 50 ns trajectory **(Fig.4A)**. This low and stable RMSD pattern indicates early achievement of conformational stability under NPT ensemble conditions (300 K, 1.01325 bar) and confirms the absence of significant structural rearrangements or domain movements during the simulation. The stable RMSD trajectory demonstrates that OPLS4 force field parameters accurately represent the protein-ligand system properties and that the simulation box configuration was appropriately designed to prevent artifacts. The ligand RMSD remained consistently below 2.0 Å throughout the entire simulation with minimal fluctuations and no evidence of systematic drift (**Fig.4B**). This remarkably stable profile indicates that **cp6** retained a highly consistent binding pose without dissociation, major positional drift, or exploration of alternative binding modes. The close alignment between protein and ligand RMSD values confirms complex structural integrity and indicates that **cp6** binding does not induce significant EGFR kinase domain conformational changes beyond local side-chain adjustments. Collectively, these RMSD data validate the cp6–EGFR complex as structurally stable over biologically relevant timescales. Root Mean Square Fluctuation (RMSF) analysis revealed expected flexibility patterns along the EGFR polypeptide chain, with higher fluctuations (RMSF > 2.5 Å) at N-terminal and C-terminal regions and solvent-exposed loop regions distant from the active site, reflecting inherent flexibility of these unconstrained segments. In contrast, the catalytic core containing α-helices and β-sheets exhibited markedly lower mobility (RMSF < 1.2 Å), confirming secondary structure preservation throughout the simulation (**Fig.4C**).

Critically, residues within the ATP-binding pocket and hinge region—particularly Met793, Asp855, Gln791, and Lys745—displayed low to moderate RMSF values (<1.5 Å), indicating maintained conformational rigidity and positional stability throughout the trajectory. The low RMSF values for Met793 and Gln791 (the gatekeeper and hinge residues) are particularly significant because flexibility in these regions typically leads to loss of ligand contacts and reduced binding affinity. The observed rigidity confirms that **cp6** binding effectively stabilizes these residues in conformations favorable for persistent interaction. Ligand RMSF analysis revealed that the core quinazoline ring system and central hydrazone linkage (–C(O)–NH–N=C–) remained largely rigid (RMSF < 0.8 Å), reflecting strong geometric constraints from conjugation, hydrogen bonding, and hydrophobic packing (**Fig.4D**). This rigidity is essential for maintaining the pharmacophoric orientation required for optimal hinge region and hydrophobic pocket interactions. In contrast, the 2,3-dihydrobenzo[b]dioxin moiety displayed minor flexibility (RMSF 1.0–1.8 Å), particularly at the ethylidene bridge.

0 This differential mobility indicates that while the ligand core remains tightly anchored through multiple stabilizing interactions, the dioxin substituent retains limited rotational freedom for favorable conformational exploration and optimized hydrophobic contacts. This localized flexibility does not compromise binding stability (as evidenced by consistently low ligand RMSD values) and may enhance binding affinity by allowing dynamic adaptation to transient binding pocket fluctuations, thereby maximizing interaction surface area and minimizing entropic penalties. Leu718 provided significant hydrophobic stabilization through sustained van der Waals contacts with the quinazoline bicyclic core and aromatic 2,3-dihydrobenzo[b]dioxin portions. Hydrophobic interaction surface area remained relatively constant (coefficient of variation < 15%), indicating minimal disruption of hydrophobic packing. Contact frequency analysis revealed that Leu718 maintained contact with **cp6** for approximately 85% of the simulation, establishing its role as a primary hydrophobic anchor. Leu788, located adjacent to the ATP-binding pocket entrance, provided additional stabilization through methyl group interactions with ligand aromatic systems, ordering surrounding water molecules and contributing to binding entropy favorability.

Critical residues Met793, Asp855, Gln791, Lys745, and Leu718 maintained frequent consistent interactions throughout the trajectory, emphasizing their molecular recognition roles and suggesting that mutations affecting these positions would significantly impact binding affinity. Ligand-protein contact timeline analysis revealed that while some contacts fluctuated transiently, the overall interaction network remained robust and redundant (**Fig.4E**). At any given timepoint, **cp6** simultaneously maintained interactions with 4–6 key residues, ensuring that transient single-contact loss did not compromise overall binding stability. This redundancy represents a hallmark of high-affinity ligand binding and suggests reduced susceptibility to resistance mutations disrupting individual contact points.

The ligand-protein interaction diagram (**Fig.4F**) categorized contacts into hydrogen bonds, hydrophobic interactions, π–π stacking, and water-mediated bridges, confirming that **cp6** engaged the EGFR active site through balanced polar and nonpolar interactions, maximizing binding enthalpy while minimizing desolvation penalties. Multiple interaction types distributed across the ligand structure reflect efficient pharmacophoric utilization, validating the rational design strategy employed for **cp6**. The 50 ns molecular dynamics simulation provided compelling multi-dimensional validation that **cp6** forms a robust, stable, and persistent EGFR kinase domain complex. Low RMSD and RMSF fluctuations, sustained hydrogen bonding, extensive hydrophobic stabilization, and adaptive interaction networks collectively demonstrate that the **cp6**–EGFR complex maintains structural stability over biologically relevant timescales (50 ns), supporting hypotheses of high conformational compatibility, favorable binding thermodynamics, and molecular recognition characteristics suitable for EGFR inhibition. These computational findings provide strong evidence supporting advancement of **cp6** into experimental validation studies, including in vitro EGFR kinase assays, cellular proliferation assays in EGFR-overexpressing cancer cell lines, and selectivity profiling against resistance-associated EGFR mutants (T790M, C797S), ultimately positioning **cp6** as a promising lead candidate for anticancer drug development targeting EGFR-driven malignancies.

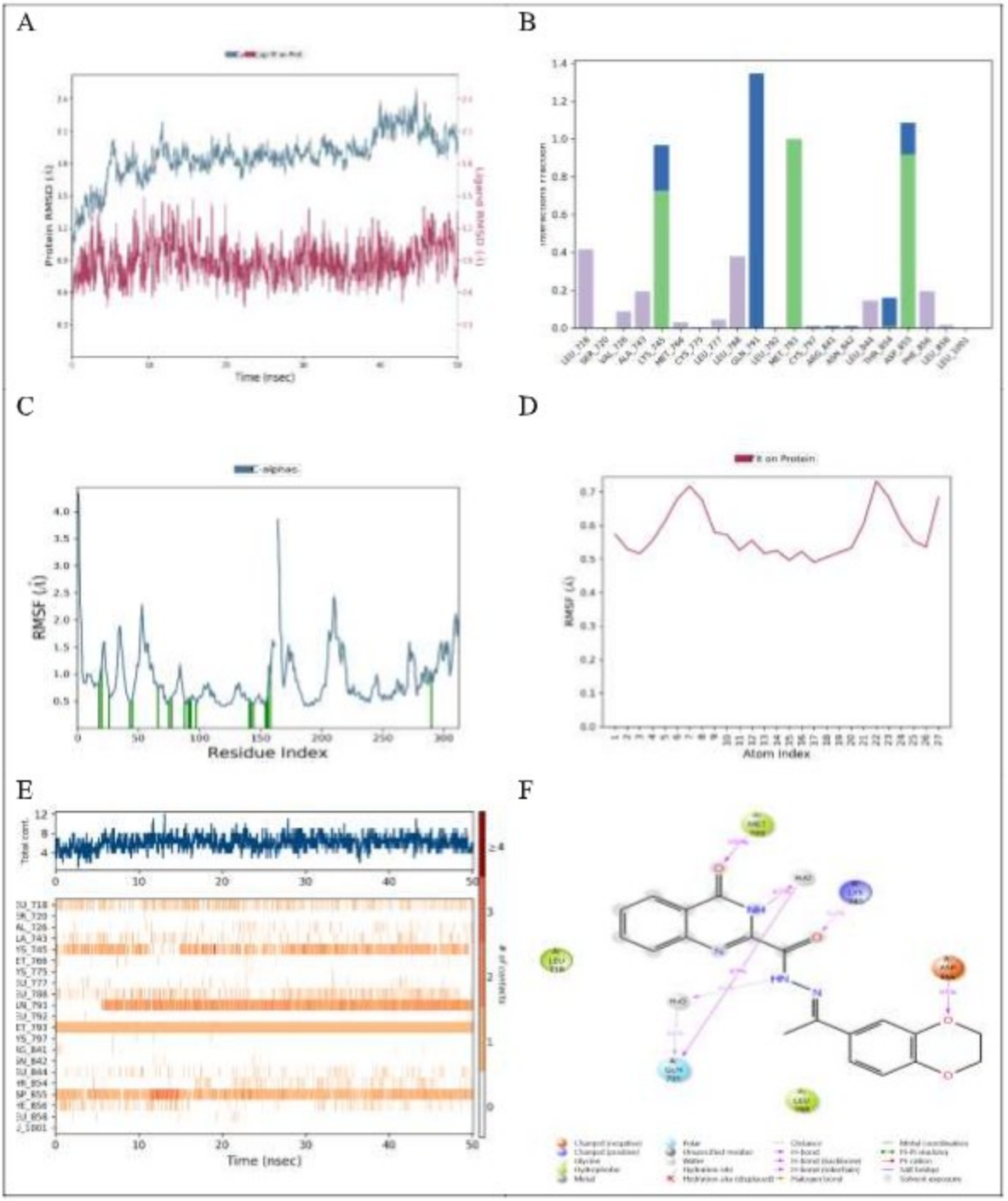

Figure4: Molecular Dynamics Analysis of **cp6**-3W33 Interactions Across Simulation Trajectory (A) Protein-Ligand RMSD; (B) Histogram of Protein-Ligand Contact Frequencies; (C) Protein RMSF; (D) Ligand RMSF; (E) Protein-Ligand Contacts; (F) Ligand-Protein Contact.

4. Conclusion

This computational investigation demonstrates that the ten rationally designed quinazoline-based derivatives (**cp1**–**cp10**) exhibit excellent drug-likeness profiles and robust EGFR binding affinities. SwissADME evaluation confirmed Lipinski's Rule of Five compliance across the series, with molecular weights of 308.29–366.37 g/mol, optimal lipophilicity (iLOGP 1.6–2.68), TPSA values of 87.21–109.33 Å², high gastrointestinal absorption, and negligible blood-brain barrier permeability, suggesting minimal CNS toxicity risk and excellent oral bioavailability potential. Molecular docking studies revealed strong binding interactions with docking scores ranging from −7.65 to −11.08 kcal/mol. Compound **cp5** exhibited the highest affinity (−11.08 kcal/mol), approaching the co-crystallized inhibitor **19b** (−11.94 kcal/mol). Critical hydrogen bonds with Met793, Tyr900, and Gly901, coupled with π–π stacking interactions and hydrophobic stabilization, validate the quinazoline scaffold as an effective EGFR pharmacophore. However, **cp6** was selected as the optimal lead candidate based on its stronger binding interaction than **cp5** as shown in Table 4, balanced ADME profile, superior hydrogen-bonding capacity (6 donors), favorable lipophilicity (2.58), synthetic accessibility, and superior resilience against EGFR resistance mutations compared to the structurally complex **cp5**. The 50 ns molecular dynamics simulation of **cp6**–EGFR complex confirmed binding stability with protein RMSD stabilizing at 1.6–2.1 Å and ligand RMSD remaining below 2.0 Å. RMSF analysis revealed minimal fluctuations (<1.5 Å) at critical residues Met793, Asp855, Gln791, and Lys745, with the quinazoline core remaining rigid (RMSF <0.8 Å). Critical hydrogen bonds and hydrophobic interactions persisted for 60–85% of the simulation, demonstrating high binding compatibility and favorable thermodynamics. These findings validate **cp6** and **cp5** as promising anticancer drug candidates warranting advancement to experimental validation through EGFR kinase inhibition assays, cellular proliferation studies in EGFR-overexpressing cancer lines, and selectivity profiling against resistance-associated mutations. The integrated computational workflow demonstrates an efficient strategy for accelerating EGFR inhibitor discovery and overcoming resistance mechanisms.

References

Abdel-Mohsen, H.T., Anwar, M.M., Ahmed, N.S., Abd El-Karim, S.S., Abdelwahed, S.H., 2024. Recent Advances in Structural Optimization of Quinazoline-Based Protein Kinase Inhibitors for Cancer Therapy (2021–Present). Molecules 29, 875. https://doi.org/10.3390/molecules29040875

Antoniolli, G., Lima, C.S.P., Coelho, F., 2025. Recent advances in the investigation of the quinazoline nucleus and derivatives with potential anticancer activities. Future Med. Chem. 17, 1193–1211. https://doi.org/10.1080/17568919.2025.2507558

Anwar, S., Alanazi, J., Ahemad, N., Raza, S., Chohan, T.A., Saleem, H., 2024. Deciphering quinazoline derivatives' interactions with EGFR: a computational quest for advanced cancer therapy through 3D-QSAR, virtual screening, and MD simulations. Front. Pharmacol. 15, 1399372. https://doi.org/10.3389/fphar.2024.1399372

Daina, A., Michielin, O., Zoete, V., 2017. SwissADME: a free web tool to evaluate pharmacokinetics, drug-likeness and medicinal chemistry friendliness of small molecules. Sci. Rep. 7, 42717. https://doi.org/10.1038/srep42717

Haloob, A., Faisal, M., Mr Raauf, A., 2024. In Silico Evaluation of Molecular Docking, Molecular Dynamic, and ADME Study of New Nabumetone Schiff Base Derivatives (1,3,4-oxadiazole or 1,3,4-thiadiazole ring) Promising Antiproliferation Action Against Lung Cancer. Turk. Comput. Theor. Chem. 8, 114–126. https://doi.org/10.33435/tcandtc.1494129

Jiménez Villalobos, T.P., Gaitán Ibarra, R., Montalvo Acosta, J.J., 2013. 2D, 3D-QSAR and molecular docking of 4(1H)-quinolones analogues with antimalarial activities. J. Mol. Graph. Model. 46, 105–124. https://doi.org/10.1016/j.jmgm.2013.10.002

Mohammadnejadi, E., Razzaghi-Asl, N., 2023. In silico target specific design of potential quinazoline-based anti-NSCLC agents. J. Biomol. Struct. Dyn. 41, 10725–10736. https://doi.org/10.1080/07391102.2023.2183029

Moussaoui, M., Baammi, S., Soufi, H., Baassi, M., Salah, M., Allali, A.E., Mohammed, B.E., Daoud, R., Belaaouad, S., 2024. Design and Optimization of Quinazoline Derivatives as Potent EGFR Inhibitors for Lung Cancer Treatment: A Comprehensive QSAR, ADMET, and Molecular Modeling Investigation. ACS Omega 9, 45842–45857. https://doi.org/10.1021/acsomega.4c04639

Şandor, A., Ionuț, I., Marc, G., Oniga, I., Eniu, D., Oniga, O., 2023. Structure–Activity Relationship Studies Based on Quinazoline Derivatives as EGFR Kinase Inhibitors (2017–Present). Pharmaceuticals 16, 534. https://doi.org/10.3390/ph16040534

Shah, A.A., Ahmad, S., Yadav, M.K., Raza, K., Kamal, M.A., Akhtar, S., 2024. Structure-based Virtual Screening, Molecular Docking, MolecularDynamics Simulation, and Metabolic Reactivity Studies ofQuinazoline Derivatives for their Anti-EGFR Activity AgainstTumor Angiogenesis. Curr. Med. Chem. 31, 595–619. https://doi.org/10.2174/0929867330666230309143711

Yadav, T.T., Moin Shaikh, G., Kumar, M.S., Chintamaneni, M., Yc, M., 2022. A Review on Fused Pyrimidine Systems as EGFR Inhibitors and Their Structure–Activity Relationship. Front. Chem. 10, 861288. https://doi.org/10.3389/fchem.2022.861288